Imaging activated T cells predicts response to cancer vaccines

Israt S. Alam,[1,2] Aaron T. Mayer,[1,2,3] Idit Sagiv-Barfi,[4] Kezheng Wang,[1,5] Ophir Vermesh,[1,2] Debra K. Czerwinski,[4] Emily M. Johnson,[1,2,6] Michelle L. James,[1,2,6] Ronald Levy,[4] and Sanjiv S. Gambhir[1,2]

[1]Department of Radiology, [2]Molecular Imaging Program at Stanford, [3]Department of Bioengineering, and [4]Division of Oncology, Department of Medicine, Stanford University, Stanford, California, USA. [5]Department of Radiology, The Fourth Hospital of Harbin Medical University and Molecular Imaging Center of Harbin Medical University, Harbin, China. [6]Department of Neurology and Neurological Sciences, Stanford University, Stanford, California, USA.

In situ cancer vaccines are under active clinical investigation, given their reported ability to eradicate both local and disseminated malignancies. Intratumoral vaccine administration is thought to activate a T cell–mediated immune response, which begins in the treated tumor and cascades systemically. In this study, we describe a PET tracer (^{64}Cu-DOTA-AbOX40) that enabled noninvasive and longitudinal imaging of OX40, a cell-surface marker of T cell activation. We report the spatiotemporal dynamics of T cell activation following in situ vaccination with CpG oligodeoxynucleotide in a dual tumor–bearing mouse model. We demonstrate that OX40 imaging was able to predict tumor responses on day 9 after treatment on the basis of tumor tracer uptake on day 2, with greater accuracy than both anatomical and blood-based measurements. These studies provide key insights into global T cell activation following local CpG treatment and indicate that ^{64}Cu-DOTA-AbOX40 is a promising candidate for monitoring clinical cancer immunotherapy strategies.

Introduction

The field of immuno-oncology has experienced rapid and exciting growth, benefiting from the development of intricate adoptive cell therapies (1) and numerous mAbs (with clinical approval of over 20 of these Abs), and a deeper understanding of the immune-suppressive tumor microenvironment now deemed a hallmark of cancer (2–4). Immunotherapies, which function by priming the patient's immune system to recognize and destroy malignant cells, have greatly altered traditional treatment paradigms. Their variable successes in the clinic have invigorated interest in non-invasive and longitudinal monitoring of immune responses, with the aim of understanding why certain therapies succeed, while others fail to deliver durable clinical responses. With the complex and varying spatiotemporal signatures of immune modulation, it has proved challenging to monitor and predict responses to cancer immunotherapy using standard imaging practices. Current clinical practice, which includes magnetic resonance–derived (MR-derived) or CT-derived anatomical measurements, often yields limited or potentially misleading data (5). With the use of MR and CT, clinicians face the challenge of distinguishing between increases in lesion size due to disease progression and "pseudoprogression" caused by an influx of tumor-infiltrating immune cells, usually a positive indicator of treatment response. Limitations to the response evaluation criteria in solid tumors (RECIST) have prompted the development of specific immune-related response criteria (irRC) (6, 7). However, even these criteria are unable to provide an early indication of therapy efficacy, such that 8–12 weeks may pass before an initial response assessment can be performed. Another limitation of these criteria is that they do not provide any biological insight. Excisional biopsies taken for histopathological assessment can yield biological information and corroborate anatomical imaging, but are invasive and challenging to apply and can be unreliable because of intrinsic tumor heterogeneity. Thus, there is a pressing need to develop predictive and prognostic readouts that can illuminate our understanding of response to immunotherapies, both in terms of dynamic alterations in immune function and clinical outcome.

PET imaging is a highly sensitive and quantitative clinical imaging modality with the potential to enable noninvasive, real-time visualization of dynamic immune responses. An array of small-molecule metabolic PET radiotracers have been developed and characterized to date for applications in immune cell imaging. For example, ^{18}F-fluorodeoxyglucose (^{18}F-FDG), the most widely used clinical PET tracer, has principally been used to assess the efficacy of traditional nontargeted chemotherapies, but has also been used extensively to evaluate inflammation in the clinic (8, 9). A major challenge in delineating immunotherapy response, however, is that ^{18}F-FDG suffers from relatively high uptake in both tumor-infiltrating T cells and cancer cells (10), as do other small-molecule metabolic tracers including 3′-deoxy-3′[^{18}F]-fluorothymidine (^{18}F-FLT), 1-(2′-deoxy-2′-[^{18}F]fluoro-β-d arabinofuranosyl)cytosine (^{18}F-AraC) (11), and 2′-deoxy-2′-[^{18}F]fluoro-9-β-D-arabinofuranosyl guanine (^{18}F-AraG) (11, 12). Reporter gene strategies, such as the use of herpes simplex virus type 1 thymidine kinase (HSV1-tk) in conjunction with the PET tracer 9-[4-[^{18}F]-fluoro-3-(hydroxymethyl)butyl] guanine (^{18}F-FHBG), represent a powerful way to monitor the traf-

Authorship note: ISA and ATM contributed equally to this work.
Conflict of interest: SSG is the founder and an equity holder of CellSight Inc., which develops and translates multimodality strategies for imaging cell trafficking and transplantation.
Submitted: November 6, 2017; **Accepted:** March 20, 2018.
Reference information: *J Clin Invest*. 2018;128(6):2569–2580.
https://doi.org/10.1172/JCI98509.

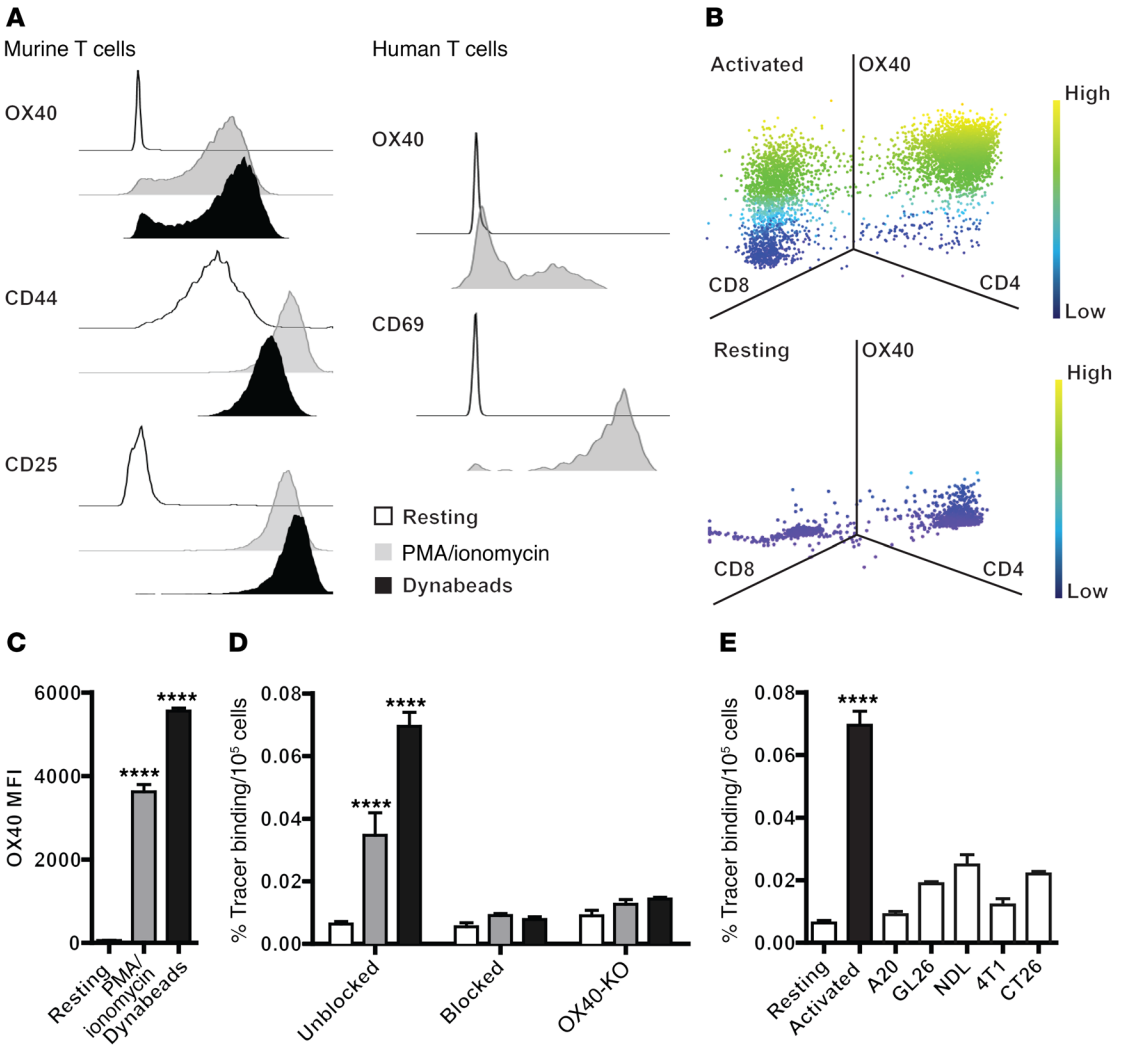

Figure 1. OX40 is a sensitive and specific indicator of T cell activation in vitro. (**A**) Histograms (fluorescence intensity) for OX40, CD44, and CD25 expression following murine T cell activation with PMA/ionomycin or CD3/CD28-specific Ab–coated Dynabeads, and histograms (fluorescence intensity) for human T cells following activation. (**B**) 3D flow cytometric plots of OX40 expression on resting and activated CD4$^+$ and CD8$^+$ murine T cell subsets. Scale bar: purple = low OX40 expression; yellow = high OX40 expression. (**C**) Quantitation of OX40 mean fluorescence intensity (MFI) of resting, PMA/ionomycin-stimulated, or Dynabead-activated murine T cells (n = 3 mice/group). (**D**) Corresponding ^{64}Cu-DOTA-AbOX40 tracer uptake (% dose/10^5 cells) in resting, PMA/ionomycin-stimulated, or Dynabead-activated murine T cells (n = 6 replicates/group) for unblocked, blocked, and KO groups from 2 independent experiments. (**E**) ^{64}Cu-DOTA-AbOX40 tracer uptake (% dose/10^5 cells) in Dynabead-activated murine T cells compared with resting T cells and various murine cancer cell lines (n = 3 mice/group). A20, B cell lymphoma; GL26, glioma; NDL, mammary carcinoma; 4T1, mammary carcinoma; CT26, colorectal carcinoma. All values represent the mean ± SEM unless otherwise specified. ****$P < 0.0001$, by 2-way ANOVA with Bonferroni's post test for group comparisons (**D**) or by 1-way ANOVA (**C** and **E**).

ficking and survival of adoptive immune cell therapies. These strategies have been evaluated clinically but require ex vivo manipulation of cells, which is not always feasible (13).

Immuno-PET, a direct imaging strategy that combines PET isotopes with targeting Abs, engineered fragments, or binders, can overcome many of the challenges associated with small-molecule radiotracers. Importantly, Immuno-PET offers increased specificity for immune subsets and functional states through the targeting of cell-surface markers (14). The presence of CD8$^+$ T cells in tumor biopsies is usually associated with a favorable therapeutic response in patients receiving immunotherapy (15, 16) and has thus fueled the development of a range of CD8-targeted PET probes (17–19). While the infiltration of CD8$^+$ T cells has been a recent major focus for the imaging community, the role of the CD4$^+$ T cell population is increasingly being reported (20, 21). A PET probe that could potentially report on both CD8$^+$ and CD4$^+$ T cell populations could therefore provide a more comprehensive picture. While CD3-targeted probes can capture the dynamics of both phenotypic subsets, this biomarker still fails to report on the activation state of T cells, which has been highlighted as a critical determinant of treatment success in oncology. Delineating cellular states such as activation and exhaustion could enable a more accurate prediction of prognostic outcomes than would reporting on the presence of tumor-infiltrating immune cells alone, which may well be present but rendered anergic. Indeed, imaging the dynamics of activated immune states is currently being explored preclinically by many groups (19, 22).

Given the explicit need for improved imaging biomarkers of response to immunotherapy and the central role of activated CD8$^+$

and CD4+ T cells in this context, our group performed a thorough literature and database query and identified the OX40 (also known as CD134) receptor as a highly promising biomarker candidate. A member of the TNF receptor superfamily, OX40 binds the ligand OX40L, found on activated antigen-presenting cells (APCs), resulting in recruitment of TNF receptor–associated factors (TRAFs), formation of a T cell receptor–independent signaling complex, and downstream activation of NF-κB (23). The resultant production of cytokines such as IL-2 and IFN-γ promotes the survival, proliferation, and activation of T cells. OX40 expression is restricted to antigen-specific activated T cells, in contrast to other activation markers (i.e., CD25, CD44) that are associated with many cell types.

Given these reports of OX40 as a highly specific biomarker of activated T cells, we set out to validate these findings by developing a PET imaging agent capable of detecting its expression. We report here for the first time to our knowledge the development of an Ab-based PET imaging agent capable of noninvasive and specific detection of OX40 for monitoring activated T cell responses in a clinically relevant in situ cancer vaccine model. Furthermore, by integrating simple machine-learning approaches and OX40 PET imaging–derived biomarkers, we successfully predict tumor response to in situ vaccines at earlier time points and with much greater accuracy than could be achieved with anatomic or blood-based biomarker strategies alone.

Results

Validation of OX40 as a sensitive and specific indicator of T cell activation. To begin, we sought to validate OX40 as a potential biomarker of activated T cells in culture. FACS analysis of murine T cells stimulated with PMA and ionomycin or with CD3- and CD28-specific Ab–coated Dynabeads showed a significant ($P < 0.001$) increase in OX40 expression compared with expression in resting cells. Importantly, we also confirmed the selective upregulation of OX40 on activated human T cells. The expression of OX40 on murine and human T cells correlated well with other established T cell activation markers including CD44, CD25, and CD69 (24, 25) (Figure 1A). A closer look at the OX40+ cells revealed that the population was composed of both CD4+ and CD8+ T cell subsets (Figure 1B).

To modify the murine OX40 Ab for radiolabeling, DOTA chelate conjugation was initially optimized using a 5-, 10-, or 15-fold excess of chelate per Ab in overnight reactions at 4°C (Supplemental Figure 1A; supplemental material available online with this article; https://doi.org/10.1172/JCI98509DS1). After conjugation, the reactions were quenched and analyzed using mass spectrometry to confirm the average number of chelates per Ab molecule. To prevent overmodification of the Ab and associated loss of immune reactivity, we chose a 5-fold DOTA excess for all subsequent batches of conjugate produced, which yielded an average of 2 to 3 DOTAs per Ab (Supplemental Figure 1B). To test immunoreactivity, we performed cell-binding studies with activated murine T cells, which showed that binding of DOTA-AbOX40 to cells was comparable to that of unconjugated Ab (Supplemental Figure 1C, left). Furthermore, using a competitive cell-binding assay, we were able to show that the endogenous OX40 ligand (OX40L) and the mAb used for tracer development do not compete, thus minimizing the potential effects of in vivo OX40L expression on radiotracer sensitivity (Supplemental Figure 1C, right). Size-exclusion chromatography–HPLC (SEC-HPLC) chromatograms of the immune conjugate at 220 nm showed a principal peak at 8 minutes, corresponding to DOTA-AbOX40, as confirmed by SDS-PAGE (Supplemental Figure 1D). Purification of the final copper-labeled immunoconjugate (^{64}Cu-DOTA-AbOX40) was followed by radio-HPLC analysis, which, in conjunction with TLC, confirmed high radiochemical purity (99%) (Supplemental Figure 1E). Final characterization of the radiotracer (^{64}Cu-DOTA-AbOX40) revealed a specific activity of 5 to 10 μCi/μg (Supplemental Figure 1F).

To assess the specificity of the radiotracer, we performed cell-binding assays using resting, PMA/ionomycin-stimulated, and Dynabead-activated murine T cells. Cells were incubated with the radiotracer for 30 minutes, washed thoroughly, and analyzed for cell-associated radioactivity using a gamma counter. ^{64}Cu-DOTA-AbOX40 binding correlated well with cell activation and OX40 expression, as measured by flow cytometry (Figure 1, C and D). Resting murine T cells, which showed negligible OX40 expression, exhibited the least amount of binding to the radiotracer. T cell activation by Dynabeads (simulating APC stimulation) is known to be a more potent stimulus for activating T cells than PMA/ionomycin. Indeed, Dynabead-activated T cells showed the greatest target expression and the correspondingly highest binding of the radiotracer (Figure 1D). Importantly, uptake was high in activated T cells and low in resting, blocked, and OX40-KO T cells, with minimal nonspecific binding in these samples. We also observed minimal nonspecific uptake across a panel of murine suspension and adherent cancer lines, providing further evidence for the high specificity of OX40 as a biomarker of activated T cells (Figure 1E).

Characterization of OX40 as a biomarker of activated T cells in an in situ adjuvant vaccine model. To establish and characterize OX40 as a biomarker of an activated T cell immune response in living subjects, we chose a model that recapitulates an in situ tumor adjuvant vaccination strategy currently being tested in phase I clinical trials (26, 27). We used a murine dual-tumor site subcutaneous A20 lymphoma model, in which an intratumoral vaccine adjuvant, CpG oligonucleotide (ODN), was administered into only 1 of the tumors. CpG ODNs are ssDNA fragments containing unmethylated cytosine-guanine sequence motifs, a signature of microbial DNA, that bind to TLRs present on APCs and trigger intracellular signaling and immune activation (28). Given its ability to elicit the innate immune component as well as antigen-specific T cell responses, CpG has been explored clinically as a vaccine adjuvant and in conjunction with chemotherapy and radiotherapy (29).

Here, mice bearing dual A20 tumors (~60–80 mm^3) were administered CpG (50 μg in 50 μl PBS) or vehicle (50 μl PBS) intratumorally on days 0, 2, and 4 at the tumor site near the left shoulder. The distal tumor on the right shoulder remained untreated (Supplemental Figure 2). We hypothesized that in situ vaccination with CpG would repolarize the locally treated tumor environment and induce an activated T cell response (Figure 2A). Tumor growth curves (volume mm^3, n = 7–8/group) indicated that CpG in situ vaccination led to a statistically significant ($P < 0.0001$, 2-way ANOVA) therapeutic response in the treated tumor as early as day 7 and delayed tumor growth in the distal untreated tumor, which was evident by day 9 ($P < 0.01$, 2-way ANOVA) (Figure 2B).

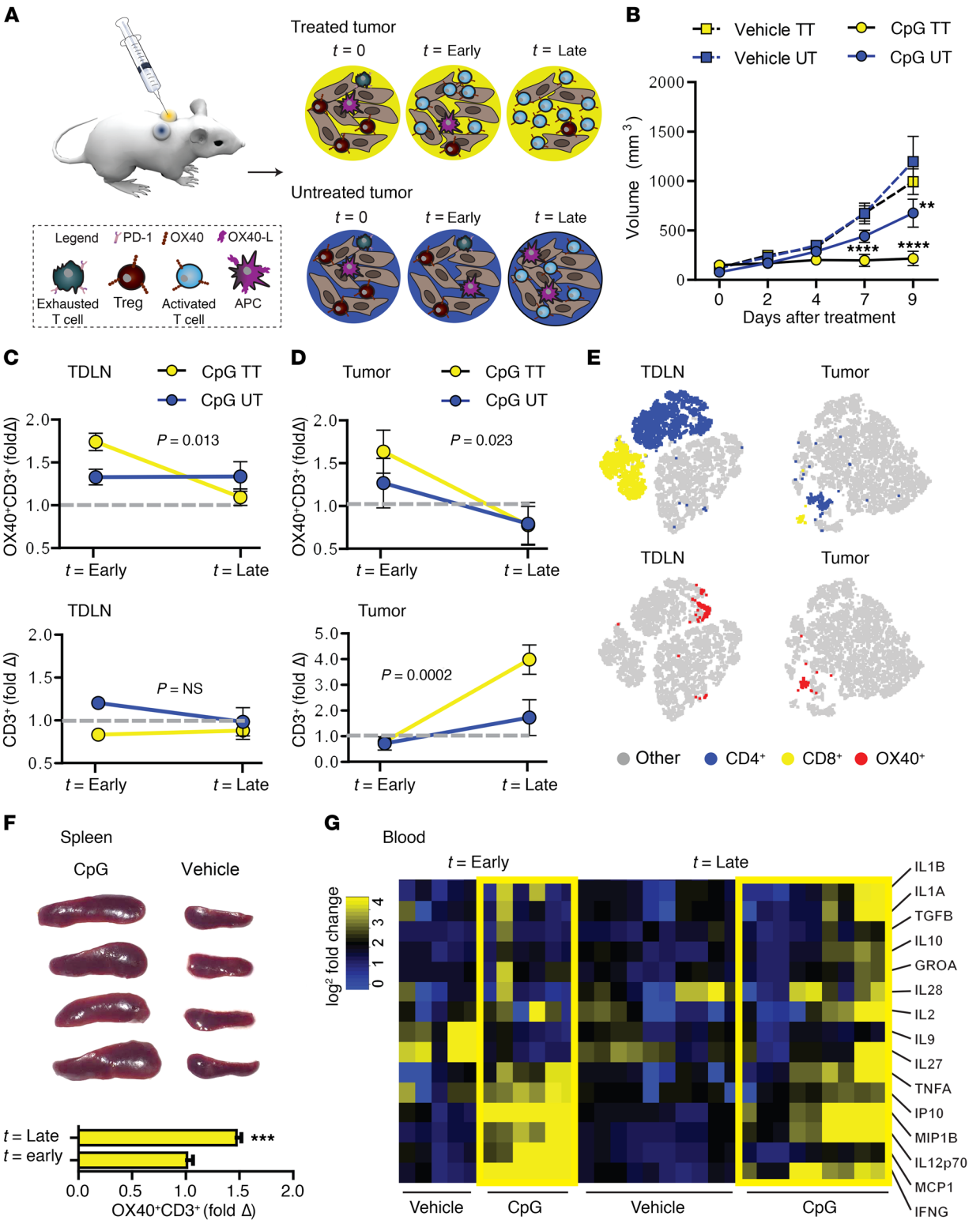
A
Treated tumor
t = 0
t = Early
t = Late
Untreated tumor
Legend
PD-1
OX40
OX40-L
Exhausted T cell
Treg
Activated T cell
APC
B
Vehicle TT
Vehicle UT
CpG TT
CpG UT
Volume (mm 3)
Days after treatment
**
****
C
TDLN
OX40+CD3+ (foldΔ)
P = 0.013
CD3+ (fold Δ)
P = NS
D
Tumor
P = 0.023
P = 0.0002
E
TDLN
Tumor
Other
CD4+
CD8+
OX40+
F
Spleen
CpG
Vehicle
t = Late
t = early
***
OX40+CD3+ (fold Δ)
G
Blood
log2 fold change
IL1B
IL1A
TGFB
IL10
GROA
IL28
IL2
IL9
IL27
TNFA
IP10
MIP1B
IL12p70
MCP1
IFNG

Figure 2. In situ vaccination with CpG activates OX40⁺ T cells in the local tumor and TDLNs, leading to the onset of a systemic response. (**A**) Schematic representation of the in situ vaccination strategy and a hypothetical immune response. (**B**) Treated tumor (TT) and untreated tumor (UT) growth curves (volume, mm^3) based on caliper measurements for CpG-treated (n = 7) and vehicle-treated (n = 8) cohorts. Values represent the mean ± SEM. ****P < 0.0001 and **P < 0.01, by 2-way ANOVA with Bonferroni's post test. (**C**) Top: Fold change (normalized to vehicle) in the frequency of OX40⁺CD3⁺ T cells in CpG-treated versus untreated TDLNs and (**D**) tumors at early (n = 5 mice/group) and late (n = 4 mice/group) time points. Bottom: Fold change in the frequency of CD3⁺ T cells. Gray dashed line demarcates unity. Values represent the mean ± SEM. Statistical analysis was performed using a 2-way ANOVA. P values represent probability differences over time in marker expression due to random chance. (**E**) Representative viSNE clustering of CD4⁺, CD8⁺, and OX40⁺ markers at the early time point in the CpG-treated cohort. (**F**) Images of spleens (late time point) from CpG- and vehicle-treated cohorts, presented side by side. Graph shows the fold change (normalized to vehicle) in the frequency of OX40⁺CD3⁺ T cells in the CpG-treated cohort at early (n = 5 mice) and late (n = 4 mice) time points. ***P < 0.001, by unpaired Student's t test. (**G**) Heatmap of $\log_2$ fold change (normalized to control mice) of cytokine expression at both early and late time points in vehicle- and CpG-treated cohorts. Columns represent mice; rows represent cytokines. Scale bars: blue = 0, yellow >4 $\log_2$ fold change.

These data suggested that the local immune response triggered by CpG had the potential to cascade systemically, in line with previous reports (26). This provided us the opportunity to characterize the spatiotemporal expression of OX40 as a potential biomarker of activated T cell immune response dynamics following in situ CpG vaccination. We chose day 2 after therapy, when no changes in tumor volume were yet evident, and day 9, when treatment cohorts exhibited a clear response stratification based on visible tumor volume reduction, as our early and late analysis time points, respectively.

At the early time point, flow cytometric analysis revealed increased OX40 expression in the treated tumor and a statistically significant increase in the frequency of OX40⁺CD3⁺ T cells following CpG in situ vaccination in the treated tumor-draining lymph node (TDLN) compared with both the untreated sites (P < 0.05) and vehicle cohorts (P < 0.01) (Figure 2, C and D, and Supplemental Figure 3, A and B). Selective upregulation of OX40 at the treatment sites alone suggested that in situ CpG vaccination triggered a local induction of a cellular immune response. Changes in OX40⁺CD3⁺ T cell frequencies preceded a relative increase in the overall proportion of CD3⁺ T cells within CpG-treated tumors. Interestingly, CpG vaccination did not cause significant changes in the relative frequencies of CD4⁺ helper or CD8⁺ cytotoxic T cell subsets within the tumor (Supplemental Figure 3, C and D).

Given the reports that OX40 expression has been found in several other cell types (30), including constitutive expression on FoxP3⁺ Tregs in mice but not humans, we examined the phenotype of cells expressing OX40 in our model. Visualization of the high-dimensional, single-cell data was performed using viSNE (described in the Supplemental Methods). viSNE maps showed OX40⁺ cells to be highly restricted to clusters associated with T cells (Figure 2E) and, more specifically, CD4⁺ helper T cells. Other potential biomarkers of T cell activation, including CD44, CD25, and PD-1, showed much less restriction to T cell–associated clusters, consistent with their known roles on a variety of other cellular subsets (Supplemental Figure 4A). OX40⁺CD4⁺ T cells in the tumor and TDLNs were also double positive for the activation markers CD44 and CD25 (Supplemental Figure 4, B and C). Furthermore, the expansion of CD44⁺CD25⁺OX40⁺CD3⁺ T cells observed upon CpG in situ vaccination represented a nonregulatory FoxP3⁻CD4⁺ T cell subset (Supplemental Figure 4D). Our analyses therefore suggest that OX40 is predominantly a biomarker of a highly activated effector T cell subset in this mouse model and that CD4⁺ T cells play an important role following in situ vaccination with CpG.

At the late time point, CpG-treated tumors showed a significant reduction in tumor volume. Correspondingly, OX40 expression returned to baseline (Figure 2, C and D). While we observed heightened OX40 expression in the distal untreated TDLNs) of a few CpG-treated mice, detectable increases in OX40 expression in the untreated tumor failed to emerge on average, consistent with a weak therapeutic response at these sites. At the late time point, secondary lymphoid organs such as the spleen appeared enlarged and showed an increase in OX40⁺CD3⁺ T cell frequencies (P < 0.001) (Figure 2F). Luminex analysis revealed that robust inflammatory cytokine signatures present in the blood on day 2 following in situ vaccination with CpG had begun to taper by day 9, with several CpG-treated mice no longer showing upregulation of inflammatory cytokines (Figure 2G, Supplemental Figure 5, and Supplemental Figure 6).

Taken together, these findings highlight the complex immune response following in situ vaccination with CpG. OX40⁺ activated T cells exhibited spatiotemporal varying signatures in response to treatment. Recognizing that biopsies are invasive and cannot adequately sample the heterogeneity in immune responses across subjects, we sought to evaluate OX40 Immuno-PET as a means of noninvasively monitoring activated T cell dynamics at the systems level.

Noninvasive imaging of OX40 to assess the spatiotemporal dynamics of activated T cells following in situ vaccination. To assess the ability of ^{64}Cu-DOTA-AbOX40 to capture the dynamics of OX40⁺ T cells and to further elucidate the critical role they play in this therapeutic model (31), we performed longitudinal Immuno-PET imaging studies. PET images acquired 24 hours after tracer injection, interestingly, showed pronounced ^{64}Cu-DOTA-AbOX40 signal in the TDLNs of tumor-bearing mice (Figure 3, Supplemental Figure 7, and Supplemental Videos 1 and 2), which we did not observe in the peripheral lymph nodes of these mice or in naive mice (data not shown). This signal is probably attributed to T cells that have been exposed to antigen draining from the local tumor or a Treg compartment that is present at baseline. Upon treatment with CpG, PET imaging (post-treatment day 2) revealed a local response to the in situ vaccination. We observed a significant enhancement of the PET signal in the CpG vaccine–treated tumor (56% increase, P < 0.01) and associated TDLNs compared with both the vehicle-treated tumor and the distal untreated sites. This observation corroborated the expansion of the OX40⁺CD4⁺ T cell effector subset we observed during our FACS studies.

Histological analysis of day-2 treated tumors supported the PET imaging findings, in which OX40-expressing cells were clearly observed in tumors receiving CpG treatment, whereas vehicle-treated tumors had overall low numbers of double-positive CD3⁺OX40⁺-stained cells, which likely represented Tregs (Supplemental Figure 8). Histology revealed a heterogeneous distribution of CD3⁺ T cell infiltration into both CpG-treated and

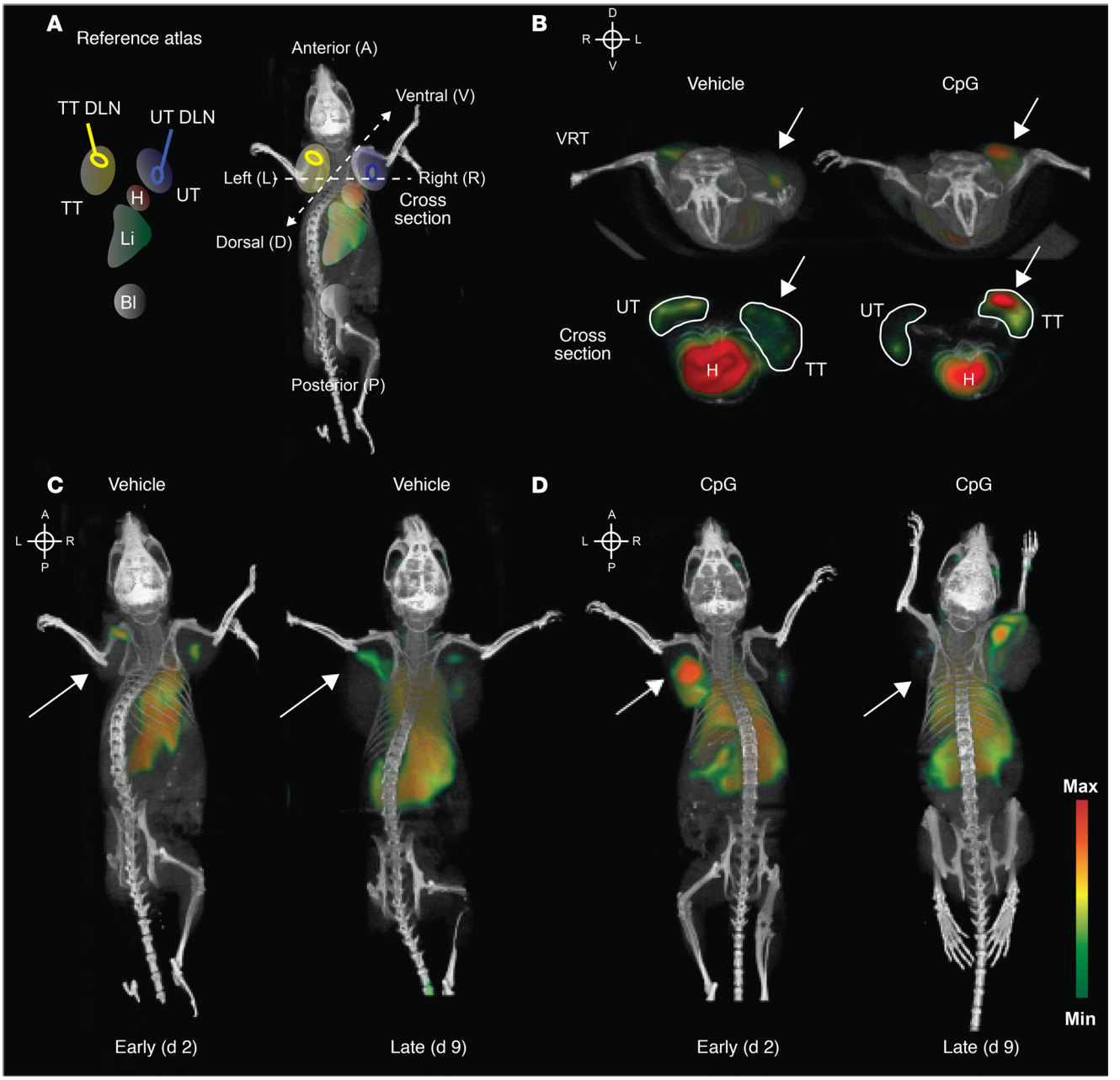

Figure 3. Noninvasive imaging of OX40 captures the spatiotemporal dynamics of activated T cells following in situ vaccination. Images were acquired 24 hours after ^{64}Cu-DOTA-AbOX40 tracer injection (~100 μCi). (**A**) Reference atlas for image ROIs. TT DLN, treated TDLN; UT DLN, untreated TDLN; H, heart; Li, liver; Bl, bladder. (**B**) Top: Head-on view of volume-rendered technique (VRT) PET-CT images of representative mice vaccinated in situ with either vehicle or CpG. Bottom: Axial cross section through tumors and heart. Images were acquired on day 2 after therapy. VRT PET-CT images of representative vehicle-treated (**C**) and CpG-treated (**D**) mice on days 2 and 9 after vaccination. White arrows indicate the treatment site. Scale bar: Maximum (Max) = red; minimum (Min) = green.

vehicle control tumors, highlighting the difficulty of assessing tumors on the basis of T cell numbers and penetration alone.

On day 9 after treatment, we observed enhancement of the ^{64}Cu-DOTA-AbOX40 PET signal in the spleen (247.9% increase, $P < 0.0001$) and in a small number of distal untreated TDLNs (Figure 3, C and D). Given that the imaging findings closely corroborate the histology and flow cytometric analysis, the evidence strongly suggests that ^{64}Cu-DOTA-AbOX40 is capable of noninvasively monitoring the dynamics of OX40$^+$ T cells.

To quantify these trends, we performed region-of-interest (ROI) analysis of multiple organs visualized on PET images as well as ex vivo biodistribution analysis. ROI analysis on day 2 revealed a distinct pattern of organ uptake in CpG-treated mice compared with that in vehicle-treated controls (Figure 4A). Moreover, unsupervised hierarchical clustering could accurately distinguish these 2 groups on the basis of their uptake signatures (Supplemental Figure 9A). Notably, we observed a greater accumulation of the tracer in CpG-treated tumors (10.29% ± 0.74 %

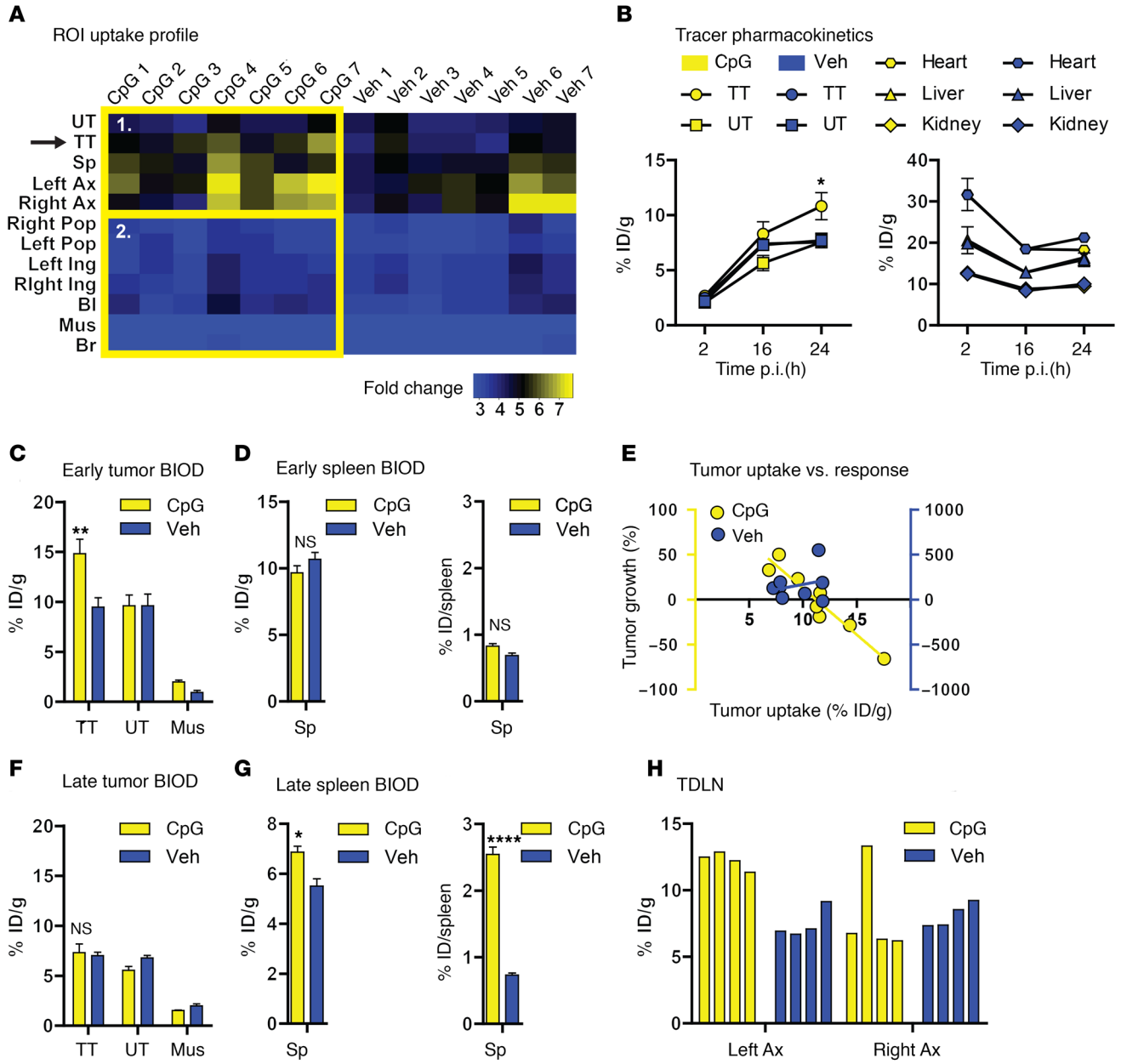

Figure 4. Quantitative Immuno-PET tracer pharmacokinetics and biodistribution. (**A**) Early (day 2) post-therapy ^{64}Cu-DOTA-AbOX40 uptake profile (fold change: % ID/g ROI/% ID/g muscle; no PVC) in CpG-treated (n = 7) versus vehicle-treated (Veh) (n = 7) mice 24 hours after injection (100 μCi). Sp, spleen; Ax, axillary LN; Pop, popliteal LN; Ing, inguinal LN; Mus, muscle; Br, brain. Two distinct clusters of image biomarkers, labeled 1 and 2, were identified from unsupervised hierarchical clustering. (**B**) ^{64}Cu-DOTA-AbOX40 pharmacokinetic uptake and clearance (% ID/g) in CpG-treated (n = 3) versus vehicle-treated (n = 3) mouse cohorts 2, 16, and 24 hours after injection (p.i.). (**C**) Early (day 2) ^{64}Cu-DOTA-AbOX40 biodistribution (BIOD) uptake (% ID/g) in treated tumors versus untreated tumors and background muscle. (**D**) Early (day 2) ^{64}Cu-DOTA-AbOX40 biodistribution uptake in spleen (% ID/g, % ID/spleen). (**E**) Early (day 2) tumor response (% change in volume) versus day-2 tumor ^{64}Cu-DOTA-AbOX40 uptake (% ID/g BIOD). Generalized linear regression was applied. CpG: $y = -10.3x + 115.3$, $R^2 = 0.9141$; vehicle: $y = 22.2x - 54.1$, $R^2 = 0.06$; y axis 1: yellow/CpG, y axis 2: blue/vehicle. (**F** and **G**) Late (day 9) ^{64}Cu-DOTA-AbOX40 uptake in tumors, spleen, and muscle (% ID/g, % ID/spleen, BIOD). (**H**) Late (day 9) uptake in left and right axillary LNs of individual CpG- and vehicle-treated mice (% ID/g, BIOD). All values represent the mean ± SEM. ****$P < 0.0001$, **$P < 0.01$, and *$P < 0.05$, by 2-way ANOVA with Bonferroni's post hoc test for multiple comparisons or by Student's t test.

injected dose per gram [ID/g], $P < 0.0001$) and associated TDLNs (12.92% ± 1.15% ID/g) versus that detected in vehicle-treated tumors (Figure 4A and Supplemental Figure 9B). To better understand the pharmacokinetics of ^{64}Cu-DOTA-AbOX40, PET signals at key sites were plotted over time (Figure 4B). Following administration, we observed that the radiotracer accumulated in all tumors over a 24-hour period; however, the CpG-treated tumors exhibited a comparatively greater increase than did vehicle-treated tumors ($P < 0.05$). In contrast to the accumulation observed in tumors, the radiotracer showed clearance from the heart, liver, and kidneys, with no significant difference in clearance from these tissues between the 2 groups.

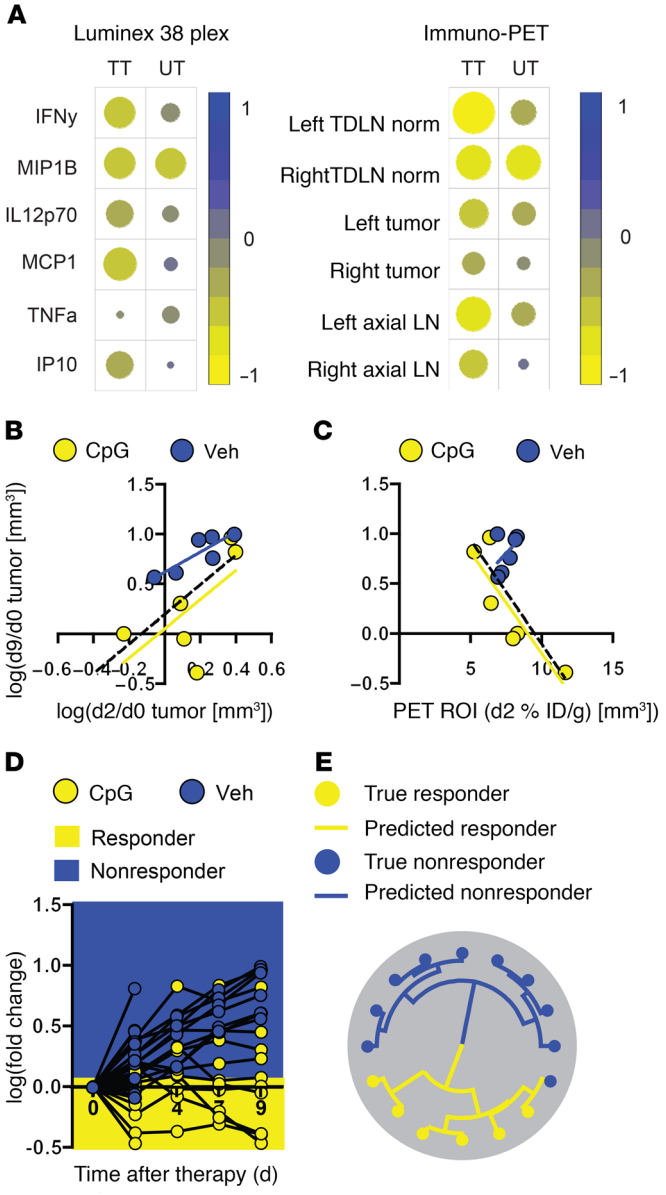

Figure 5. Imaging- and blood-based correlates of response to in situ tumor vaccination with CpG. (**A**) Correlelogram of top hits determined by significance analysis of microarrays from a Luminex 38 plex cytokine assay (fold change; MFI/control) and Immuno-PET imaging ROIs (fold change; % ID/g ROI/muscle) with tumor response on day 2: log(fold[tumor volume mm^3 on day 2/tumor volume mm^3 on day 0]). Color scale and circle size both represent Pearson's correlation coefficients. Large yellow circle (–1) indicates perfect inverse correlation; no circle (0) indicates no correlation; large blue circle (1) indicates perfect correlation. (**B**) Univariate regression of day-9 tumor response versus day-2 tumor response according to anatomical measurements. (**C**) Univariate regression of day-9 tumor response versus day-2 tumor tracer uptake (% ID/g). Blue line indicates vehicle-only fit; yellow line indicates CpG-only fit; black dashed line indicates all. (**D**) Tumor growth versus time after therapy. Yellow zone designates responders. The cutoff was determined using unsupervised hierarchical clustering. (**E**) Unsupervised hierarchical clustering and model visualization of the k-means nearest-centroid classifier. Lines indicate predictions; circles indicate truth.

Ex vivo analysis of tissues on day 2 also corroborated the imaging data (Supplemental Figure 9, B and C). We observed a significant increase in radioactivity between treated tumors in the experimental versus the vehicle-treated groups ($P < 0.01$), with no significant differences in the distal untreated tumors between the 2 groups (Figure 4C). Differences observed between groups appeared to be local at this time point, with no splenic involvement (Figure 4D). Blocking with a cold Ab significantly reduced ^{64}Cu-DOTA-AbOX40 uptake in the CpG-treated tumors as well as in the TDLNs, in this case, the axillary LNs (AX LN, Supplemental Figure 9B), confirming the specificity of the PET signal for OX40. We observed a strong inverse correlation between tumor response (measured as a decrease in tumor volume) and tracer uptake in tumors on day 2 (Figure 4E).

On day 9, however, we found that tracer uptake was no longer increased in the CpG-treated tumors relative to the vehicle-treated tumors, while the spleens of the experimental group showed a significant increase in tracer accumulation compared with that in the vehicle-treated group (Figure 4, F and G). The signal in the CpG-treated TDLNs (Left Ax, Figure 4H) showed persistent enhancement, and, as before, only rarely tracer accumulation enhanced in the nontreated TDLNs (Right Ax, Figure 4H).

To thoroughly test the specificity of our imaging agent, we used additional controls (Supplemental Figure 9, D and E). For example, in 1 experiment, we injected a nonradiolabeled isotype control Ab prior to radiotracer administration in order to rule out nonspecific uptake of the radiotracer resulting from Fc receptor upregulation in response to CpG treatment. The lack of blocking in the CpG-treated tumors of mice pretreated with the isotype control demonstrates that Fc receptors do not contribute significantly to tracer binding in the tumor and TDLN and that the tracer accumulation occurs principally through engagement with OX40. In a separate experiment, we treated an OX40-KO melanoma tumor–bearing mouse model with the same vaccine strategy. Unlike OX40 WT mice, which showed a statistically significant 1.4- to 1.5-fold increase ($P < 0.05$) in tracer uptake in CpG-treated versus distal untreated tumors, OX40-KO mice failed to show this trend, despite responding to the CpG therapy (Supplemental Figure 9E).

Classification and prediction of tumor response to in situ vaccination using in vivo OX40 imaging biomarkers. Having established that ^{64}Cu-DOTA-AbOX40 could report on activated T cell immune responses with high sensitivity and specificity, our final goal was to compare and contrast the ability of blood- and image-derived biomarkers to monitor and predict tumor response. We therefore performed profiling of blood cytokines and image ROIs to identify biomarkers that correlate with tumor response (Figure 5A). Individual cytokines and cytokine sets showed weak correlation with tumor response (Table 1), whereas imaging biomarkers alone showed an improved correlation. Incorporating multiple PET imaging biomarkers into our generalized linear regression model yielded a statistically significant correlation with therapeutic response ($R^2 = 0.674$, $P = 8.425 \times 10^{-5}$) (Table 1).

We further set out to determine whether early (day 2) Immuno-PET images could provide insight into a late (day 9) therapeutic response. Anatomical measurements revealed that an early tumor response to CpG was not a strong predictor of a late therapeutic response ($R^2 = 0.40$, $P = 0.18$), with some tumors showing initial regression followed by growth and others presenting with pseudo-

Table 1. Correlates of early tumor response

	PET (n = 28)	Luminex (n = 12)
Model	Multi GLM	Mul GLM
y	log(d2/d0 mm^3)	log(d2/d0 mm^3)
×1, ×2, ×3 ...	See legend	See legend
Res. standard error	0.162	0.127
Degrees of freedom	22	7
R^2	0.674	0.405
P value	8.425×10^{-5}	0.393

Multi GLM, multivariate general linear regression model. PET predictors ×1, ×2, ×3: TDLN normalized to tumor size (mean % ID/g: mm^3), tumor (mean % ID/g), axillary LN (mean % ID/g), inguinal LN (mean % ID/g), popliteal LN (mean % ID/g). Luminex predictors ×1, ×2, ×3: IFN-γ, MIP1B, IL-12p70, MCP1 (n = number of tumors).

progression (Figure 5B and Table 2). On the other hand, we found that early Immuno-PET tracer uptake in tumors was strongly correlated with a late therapeutic response in CpG-treated mice (R^2 = 0.76, P = 0.02) (Figure 5C and Table 2). Given the large discrepancies in tumor volumes between CpG- and vehicle-treated cohorts, we initially considered them independently. As expected, vehicle-treated mice showed a correlation between early and late anatomical measurements (R^2 = 0.74, P = 0.11), while early Immuno-PET tracer uptake in tumors did not correlate with a late response (R^2 = 0.23, P = 0.33). Incorporating multiple OX40 image-derived biomarkers into our linear regression provided us with a robust general model (R^2 = 0.74, P = 0.08) with which to assess the response, independent of the treatment cohort.

Finally, we sought to determine whether our Immuno-PET images could enable accurate classification of therapeutic responders versus nonresponders. We stratified mice into 2 response groups with the help of unsupervised hierarchical clustering (Figure 5D). We built a simple k-means classifier based on our imaging biomarkers, which we had previously identified to correlate well with a therapeutic response (Figure 5E). We trained the classifier on a subset of mice (n = 16) and tested the classifier on all cohorts of mice included in our study (n = 46). The model performed well, with 83% accuracy, 82% specificity, and 85% sensitivity in the total cohort (Table 3). Overall, we view this as an initial and promising proof of principle that OX40 Immuno-PET image–derived biomarkers can not only monitor, but also classify, responders at early time points following therapy.

Table 2. Predictors of late tumor response

	Anatomical (n = 12)	PET (n = 12)	PET (n = 12)
Model	Uni GLM	Uni GLM	Multi GLM
Vehicle (R^2/P value)	0.74/0.11	0.23/0.33	NA
CpG (R^2/P value)	0.40/0.18	0.76/0.02	NA
All (R^2/P value)	0.34/0.05	0.39/0.03	0.74/0.08

Correlation coefficient R^2 and P values for model fits. Uni GLM, univariate general linear regression model. n = number of tumors.

Discussion

Given the relative ease of Immuno-PET tracer development, it is feasible to build a clinical toolbox of tracers useful for predicting and monitoring responses to different cancer immunotherapies. Here, we highlight the development cycle starting from biomarker identification (OX40) and tracer development (^{64}Cu-DOTA-AbOX40) to biomarker characterization and tracer validation in mouse models treated with immunotherapy. Moreover, we demonstrate the potential clinical utility of this tracer by illustrating its predictive power in therapeutic mouse models, a critical step often omitted from many preclinical imaging studies.

As the field evolves and an imaging toolbox to assess immunotherapies is developed, careful biomarker selection is paramount. Small-molecule tracers, as previously mentioned, have focused on metabolic pathways that are not immune cell specific. Nucleoside analogs like ^{18}F-FLT, ^{18}F-AraC, and ^{18}F-AraG have all been explored for immune cell imaging (11, 12, 32). The latter, for instance, has increased specificity for activated T cells (33) and recently showed utility in the detection of these cells in murine models of acute graft versus host disease (GVHD) and arthritis (34). In the context of cancer, however, with the uptake mechanism of these metabolic tracers being dependent on elevated levels of nucleoside transporters and DNA salvage pathway enzymes, imaging of tumor-infiltrating T cells could potentially be confounded by uptake in certain cancers that exhibit the same features. Meanwhile, previous Immuno-PET strategies have struggled to demonstrate utility, because the presence of infiltrating immune cell subsets does not on its own correlate well with immune response (18). In addition, while imaging metrics of cell infiltration have been developed, their use may prove difficult when applied in the clinic, given the heterogeneity, size, and shape of spontaneous tumors. Imaging markers that directly reflect the functional status of specific cells have the potential to be more predictive, provided that expression profiles of those markers are well characterized and their role within the context of a particular disease is well understood.

Imaging can be used to help characterize these roles. In this study, we demonstrate that noninvasive imaging of OX40$^+$ activated T cells has the potential to be a suitable biomarker of early response in cancer immunotherapy. We also describe the successful development of an Immuno-PET agent, ^{64}Cu-DOTA-AbOX40, which is capable of detecting OX40 expression with high sensitivity and specificity. We chose a murine OX40–specific IgG1, which, upon modification with DOTA, retained its immune reactivity. Bioconjugation and subsequent radiolabeling with copper-64 were both easy and reproducible. Cell culture and in vivo binding of the radiotracer directly correlated with expression of the biological target, as rigorously characterized by FACS analysis. In our in vivo studies using a murine dual-tumor site subcutaneous lymphoma model, in which an intratumoral vaccine of CpG was administered into only 1 of the tumors, we found that CD4$^+$OX40$^+$ T cells played an important role in the local tumor and TDLNs following vaccination with in situ CpG. The expansion of this OX40$^+$ T cell subset may further benefit from combination therapy with an OX40 agonist, as recently demonstrated by Sagiv-Barfi et al. (35). The authors of the study also demonstrated that CpG does not increase CTLA-4 or PD-1 expression and that an OX40 agonist alone signifi-

Table 3. Classification of responders versus nonresponders

	Train (*n* = 16)	Test (*n* = 30)	Total (*n* = 46)
Model	k-means	k-means	k-means
Accuracy	0.938	0.767	0.826
Sensitivity	0.90	0.71	0.85
Specificity	1.00	0.78	0.82

Accuracy, sensitivity, and specificity of training (*n* = 16), testing (*n* = 30), and total (*n* = 46) included in the study. *n* = number of tumors.

cantly boosts therapeutic efficacy and leads to complete tumor eradication (35). More recent work has shown that the timing of PD-1 administration can either aid or impair treatment with OX40 (36). As demonstrated here, Immuno-PET can provide insight into these spatiotemporal dynamics and help drive rational drug development and combination strategies.

To realize the full power of Immuno-PET and improve clinical decision making, image-derived biomarkers should ideally be combined with other blood-based biomarkers and genetic tests. Utilizing multiple image-derived biomarkers is especially important when imaging an immune response, in which sites such as LNs and spleen can provide additional clues to a patient's therapeutic response. The classifier used in this work is only a simple proof of concept, and we plan to test support vector machines and other approaches to determine whether we can further refine the outcome. Blood-based biomarkers performed poorly in the context of monitoring multiple lesions. By contrast, the whole-body spatial information that imaging provides is especially important when utilizing in situ approaches, in which the optimal follow-up may warrant injection into nonresponding sites. Integrating blood, tissue biopsy, and imaging assays with improvements in computational and statistical learning algorithms represents a powerful diagnostic and prognostic patient management approach.

Our data identify OX40 as a highly promising biomarker for imaging-activated T cells in vivo, with OX40 Immuno-PET representing a readily translatable strategy that can be integrated into the clinical workflow to aid the prediction of response, possibly much earlier than current methods allow. The murine Ab imaging strategy described here can be readily adapted to human Abs against OX40 that are being used for therapy for OX40 imaging in the clinic. The potential of this strategy could also extend beyond immunotherapies, with utility in a number of T cell–driven disease indications such as multiple sclerosis (37) and GVHD (38, 39), in which expression of this marker has been reported. Immuno-PET strategies will further benefit from the development of second-generation agents such as engineered binders that have improved pharmacokinetic properties (e.g., faster blood clearance, lower hepatic accumulation) and are compatible with shorter-lived isotopes, allowing one to image soon after administering the tracer and achieve a higher signal-to-background ratio. We are currently pursuing these other avenues to address the breadth of possible applications in a number of disease models. Given the promise shown in these preclinical studies, we have started on the clinical translation of OX40 Immuno-PET.

Methods

Study design. The primary objective of this study was to develop an imaging agent (^{64}Cu-DOTA-AbOX40) to noninvasively measure OX40 expression with PET imaging in a dual-tumor mouse model treated with an in situ adjuvant vaccine. Mice with dual A20 tumors were size matched before treatment initiation and received either CpG or vehicle in the left shoulder tumor alone. Tumor volumes of both treated and distal untreated tumors were measured periodically in mice from both treatment groups to monitor the treatment response. Five to seven mice per treatment group were used for PET evaluation of OX40 expression at early and late time points after treatment initiation. Additionally, at the same time points, a separate cohort was analyzed by FACS to evaluate OX40 expression and by Luminex assay for the measurement of cytokines in the blood. All outliers were included in the analysis, and no data were excluded. The investigators were not blinded to the results. A minimum of 3 experimental replicates were recorded for all in vitro data. Simple or multiple linear regression models were used to assess the correlation of biomarkers with outcomes. Unsupervised hierarchical clustering was used to assign group labels (i.e., responder and nonresponder) on the basis of tumor growth curves. A k-means nearest-centroid approach was used to classify tumors on the basis of imaging biomarkers.

DOTA conjugation and conjugate characterization. OX40-DOTA conjugation was performed with DOTA-NHS (Macrocyclics) using previously described established protocols (40). Briefly, DOTA conjugation was first optimized using the murine OX40 mAb (clone OX86; BioXcell) resuspended in PBS at 0.5 mg/ml and then buffer exchanged into metal-free HEPES buffer (pH 8.8), followed by incubation overnight at 4°C with a 5-, 10-, or 15-fold excess of DOTA-NHS. The reactions were quenched with Tris buffer, buffer exchanged into metal-free water to remove excess DOTA-NHS, and concentrated. An aliquot of this solution was set aside for matrix-assisted laser desorption ionization–time-of-flight mass spectometry (MALDI-TOF) analysis along with a sample of unconjugated OX40 Ab to characterize the average number of chelators per Ab molecule. Briefly, the mean DOTA/mAb ratio was determined by calculating the change in mass seen with MALDI using the AB Sciex 5800 TOF/TOF machine (AB Sciex) equipped with a CovalX high-mass detector, divided by the mass of a single DOTA substituent. An average ratio of 1:3 DOTAs per Ab was achieved for the 5-fold excess DOTA reaction and used for all subsequent conjugation reactions. Following MALDI, the solution of DOTA-OX40 mAb was buffer exchanged into ammonium acetate buffer (0.1 M, pH 5.5) for copper-64 labeling. DOTA-conjugate solutions were concentrated using ammonium acetate by ultrafiltration (2 ml; Vivaspin; Sartorius) to 2 to 3 mg/ml and stored at 4°C prior to radiolabeling.

Radiolabeling studies. Standard procedures were used to radiolabel OX40-DOTA with $^{64}CuCl_2$ (University of Wisconsin, Madison, Wisconsin, USA) (40). ^{64}Cu-DOTA-AbOX40 was produced with a specific activity of 5 to 10 μCi/μg, with high radiochemical purity (>99%) and labeling efficiency of 60% to 75%, as determined by thin-layer chromatography (TLC). Radio-HPLC was performed to corroborate labeling of the Ab. The final formulation was made up in PBS (0.1 mol/l NaCl, 0.05 M sodium phosphate, pH 7.4).

In brief, DOTA-OX40-mAb (100 μg) in 0.25 mol/l ammonium acetate buffer (0.1 M, pH 5.5) was mixed with pH-balanced $^{64}CuCl_2$ solution (37 MBq, pH 5.0–5.5; University of Wisconsin) at 37°C with

gentle shaking at 300 rpm. After a 60-minute incubation period, 0.1 M EDTA (0.5 M, pH 8.0) was added to a final concentration of 0.01 M and incubated at room temperature for 15 minutes to scavenge unchelated $^{64}CuCl_2$ in the reaction mixture. Purification of ^{64}Cu-DOTA-OX40-mAb was achieved by G25 Sephadex size-exclusion purification (NAP-5 column). Radiochemical purity was determined by instant TLC with TEC-Control Chromatography Strips (Biodex Medical Systems) developed in saline, followed by size-exclusion liquid chromatography with a Phenomenex SEC 3000 column with sodium phosphate buffer (0.1 mol/l, pH 6.8) at a flow rate of 1.0 ml/min.

In situ vaccine mouse model. Six- to eight-week-old female BALB/c mice were purchased from Charles River Laboratories. A20 cells (10×10^6) were implanted subcutaneously into the left and right shoulders. Once tumors had grown to approximately 60 to 80 mm^3 in size, mice were treated in their left shoulder tumor with either 50 μg CpG (SD101 oligonucleotide; Dynavax Technologies) or 50 μl PBS. Mice in the control group received a 50-μl injection of PBS into the left shoulder tumor. Two days after treatment initiation (early therapy time point), the mice were subjected to PET imaging, FACS, or Luminex analysis. A separate cohort of mice also underwent 2 repetitions of the same intratumoral vaccines on days 2 and 4 after the first treatment. These mice were also used for PET imaging, FACS, or Luminex analysis on day 9 after administration of the first treatment (late therapy time point).

Small animal PET-CT, biodistribution studies, and image analysis. Small animal PET-CT was performed using a previously reported protocol (40). Mice were anesthetized using isoflurane gas (2.0%–3.0% for induction and 1.5%–2.5% for maintenance). ^{64}Cu-DOTA-AbOX40 (80–110 μCi) was administered intravenously via the tail vein 24 hours after intratumoral injections. Two types of blocking studies were performed: (a) Anti-mouse OX40 mAb (100 μg; BioXCell) was administered intravenously 30 minutes before radiotracer administration (n = 3 CpG-treated mice); and (b) a separate cohort of mice (n = 4 per treatment group) received anti-HRP rat IgG1 isotype control (100 μg; BioXCell) 15 minutes prior to radiotracer administration to further demonstrate specificity of the probe and rule out the contribution of the radiotracer binding to Fc receptors rather than to the OX40 target, since CpG treatment leads to increased Fc receptor expression (41).

Static PET scans (10-min) were acquired 4, 16, and 24 hours after ^{64}Cu-DOTA-AbOX40 administration. CT images were acquired just before each PET scan to provide an anatomic reference for and attenuation correction of the PET data. Following completion of the scan 24 hours after tracer administration, biodistribution studies were performed to measure blood- and tissue-associated radioactivity. Briefly, blood was collected via cardiac puncture, and various tissues including left (treated) and right (untreated) tumors, left and right TDLNs, inguinal LNs, kidney, liver, lung, muscle, bone, and spleen were collected and weighed, and radioactivity was measured using an automated gamma counter (Cobra II; Packard). Radioactivity was decay corrected to the time of radiotracer injection using diluted aliquots of the initial administered dose as standards. Data are expressed as a percentage of the injected dose per gram of tissue (% ID/g).

All PET images were reconstructed using 2 iterations of a 3D ordered subsets expectation maximization algorithm (12 subsets) and 18 iterations of the accelerated version of 3D-MAP (i.e., FASTMAP), with a matrix size of 128 × 128 × 159. Attenuation correction was applied to the data set from the CT image. For quantitation, PET images were coregistered with CT images to generate fused images using Inveon Research Workplace (IRW) image analysis software, version 4.0 (Siemens). The PET images were analyzed with IRW software, version 4.0. The CT images were used to guide the drawing of 3D ROIs around the left and right tumors, TDLNs, muscle, kidney, and liver. The percentage of injected dose per gram was calculated for each ROI. Partial volume correction (PVC) was not applied.

To analyze the pharmacokinetics of ^{64}Cu-DOTA-AbOX40, ROIs were drawn over key sites — tumor, heart, liver, and kidney — in the scans acquired for both treatment groups 4, 16, and 24 hours after tracer administration. PET signal (% ID/g) for these key sites were plotted over time to observe accumulation or clearance.

Statistics. General statistical analyses were performed using GraphPad Prism 5.0 (GraphPad Software). An unpaired, 2-tailed Student's t test, 1-way ANOVA, or 2-way ANOVA was used for column, multiple column, and group analyses, respectively. A Bonferroni's post test was applied when appropriate to correct for multiple comparisons. P values of less than 0.05 were considered statistically significant. Simple linear regression models were generated in GraphPad Prism, while multiple linear regressions were performed in R. Pearson's correlation coefficients and P values were calculated and reported for all model fits.

Study approval. All procedures performed on animals were approved by the IACUC of Stanford University and were in accordance with NIH guidelines for the humane care of laboratory animals.

Author contributions

ISA and ATM conceived and designed research studies, developed methodology, conducted experiments, acquired data, analyzed data, and prepared the manuscript. ISB and DKC developed methodology, conducted experiments, and analyzed data. KW and OV conducted experiments. EMJ and MLJ developed methodology and provided technical and conceptual advice. RL conceived and designed research studies. SSG conceived and designed research studies and prepared the manuscript.

Acknowledgments

The authors would like to acknowledge the Stanford Center for Innovation in In-Vivo Imaging (SCI[3]) and, in particular, Timothy Doyle and Frezghi Habte for their assistance with the preclinical imaging experiments and image analyses. We also thank members of the Stanford FACS facility and the Stanford Human Immune Monitoring Core for their expertise. In addition, we thank Kenneth Lau for assistance with mass spectrometry and Seung Min-Park (both from the Department of Radiology, Stanford University) for help with the preparation of this manuscript. This work was supported in part by funding from the Ben and Catherine Ivy Foundation (to SSG); the Canary Foundation (to SSG); the National Cancer Institute (NCI) (R01 1 CA201719-02, to SSG); and the Leukemia and Lymphoma Society (TAP-120921, to RL).

Address correspondence to: Sanjiv Sam Gambhir, Department of Radiology, Stanford University, The James H Clark Center, 318 Campus Drive, East Wing 1st Floor, Stanford, California 94305, USA. Phone: 650.725.2309; Email: sgambhir@stanford.edu.

1. Berraondo P, et al. Cellular immunotherapies for cancer. *Oncoimmunology*. 2017;6(5):e1306619.
2. Kim S, Moon EK. Development of novel avenues to overcome challenges facing CAR T cells. *Transl Res*. 2017;187:22–31.
3. Finn OJ. Immuno-oncology: understanding the function and dysfunction of the immune system in cancer. *Ann Oncol*. 2012;23 Suppl 8:viii6–viii9.
4. Hanahan D, Weinberg RA. Hallmarks of cancer: the next generation. *Cell*. 2011;144(5):646–674.
5. Neves AA, Brindle KM. Assessing responses to cancer therapy using molecular imaging. *Biochim Biophys Acta*. 2006;1766(2):242–261.
6. Wolchok JD, et al. Guidelines for the evaluation of immune therapy activity in solid tumors: immune-related response criteria. *Clin Cancer Res*. 2009;15(23):7412–7420.
7. Hodi FS, et al. Evaluation of Immune-Related Response Criteria and RECIST v1.1 in Patients With Advanced Melanoma Treated With Pembrolizumab. *J Clin Oncol*. 2016;34(13):1510–1517.
8. Basu S, Chryssikos T, Moghadam-Kia S, Zhuang H, Torigian DA, Alavi A. Positron emission tomography as a diagnostic tool in infection: present role and future possibilities. *Semin Nucl Med*. 2009;39(1):36–51.
9. Stelljes M, et al. Clinical molecular imaging in intestinal graft-versus-host disease: mapping of disease activity, prediction, and monitoring of treatment efficiency by positron emission tomography. *Blood*. 2008;111(5):2909–2918.
10. Laing RE, Nair-Gill E, Witte ON, Radu CG. Visualizing cancer and immune cell function with metabolic positron emission tomography. *Curr Opin Genet Dev*. 2010;20(1):100–105.
11. Radu CG, et al. Molecular imaging of lymphoid organs and immune activation by positron emission tomography with a new [18F]-labeled 2'-deoxycytidine analog. *Nat Med*. 2008;14(7):783–788.
12. Ronald JA, et al. A PET Imaging Strategy to Visualize Activated T Cells in Acute Graft-versus-Host Disease Elicited by Allogenic Hematopoietic Cell Transplant. *Cancer Res*. 2017;77(11):2893–2902.
13. Keu KV, et al. Reporter gene imaging of targeted T cell immunotherapy in recurrent glioma. *Sci Transl Med*. 2017;9(373):aag2196.
14. Freise AC, Wu AM. In vivo imaging with antibodies and engineered fragments. *Mol Immunol*. 2015;67(2 Pt A):142–152.
15. Galon J, et al. Type, density, and location of immune cells within human colorectal tumors predict clinical outcome. *Science*. 2006;313(5795):1960–1964.
16. Klein O, et al. Melan-A-specific cytotoxic T cells are associated with tumor regression and autoimmunity following treatment with anti-CTLA-4. *Clin Cancer Res*. 2009;15(7):2507–2513.
17. Tavaré R, et al. An effective Immuno-PET imaging method to monitor CD8-dependent responses to immunotherapy. *Cancer Res*. 2016;76(1):73–82.
18. Rashidian M, et al. Predicting the response to CTLA-4 blockade by longitudinal noninvasive monitoring of CD8 T cells. *J Exp Med*. 2017;214(8):2243–2255.
19. Larimer BM, et al. Granzyme B PET Imaging as a Predictive Biomarker of Immunotherapy Response. *Cancer Res*. 2017;77(9):2318–2327.
20. Spitzer MH, et al. Systemic immunity is required for effective cancer immunotherapy. *Cell*. 2017;168(3):487–502.e15.
21. Zanetti M. Tapping CD4 T cells for cancer immunotherapy: the choice of personalized genomics. *J Immunol*. 2015;194(5):2049–2056.
22. Di Gialleonardo V, Signore A, Glaudemans AW, Dierckx RA, De Vries EF. N-(4-18F-fluorobenzoyl) interleukin-2 for PET of human-activated T lymphocytes. *J Nucl Med*. 2012;53(5):679–686.
23. Willoughby J, Griffiths J, Tews I, Cragg MS. OX40: Structure and function - what questions remain? *Mol Immunol*. 2017;83:13–22.
24. Huet S, Groux H, Caillou B, Valentin H, Prieur AM, Bernard A. CD44 contributes to T cell activation. *J Immunol*. 1989;143(3):798–801.
25. Wieland E, Shipkova M. Lymphocyte surface molecules as immune activation biomarkers. *Clin Biochem*. 2016;49(4-5):347–354.
26. Marabelle A, Kohrt H, Caux C, Levy R. Intratumoral immunization: a new paradigm for cancer therapy. *Clin Cancer Res*. 2014;20(7):1747–1756.
27. Wang S, et al. Intratumoral injection of a CpG oligonucleotide reverts resistance to PD-1 blockade by expanding multifunctional $CD8^+$ T cells. *Proc Natl Acad Sci U S A*. 2016;113(46):E7240–E7249.
28. Hanagata N. CpG oligodeoxynucleotide nanomedicines for the prophylaxis or treatment of cancers, infectious diseases, and allergies. *Int J Nanomedicine*. 2017;12:515–531.
29. Brody JD, et al. In situ vaccination with a TLR9 agonist induces systemic lymphoma regression: a phase I/II study. *J Clin Oncol*. 2010;28(28):4324–4332.
30. Weinberg AD, Morris NP, Kovacsovics-Bankowski M, Urba WJ, Curti BD. Science gone translational: the OX40 agonist story. *Immunol Rev*. 2011;244(1):218–231.
31. Marabelle A, et al. Depleting tumor-specific Tregs at a single site eradicates disseminated tumors. *J Clin Invest*. 2013;123(6):2447–2463.
32. Yue J, et al. Measuring tumor cell proliferation with 18F-FLT PET during radiotherapy of esophageal squamous cell carcinoma: a pilot clinical study. *J Nucl Med*. 2010;51(4):528–534.
33. Namavari M, Chang YF, Kusler B, Yaghoubi S, Mitchell BS, Gambhir SS. Synthesis of 2'-deoxy-2'-[18F]fluoro-9-β-D-arabinofuranosylguanine: a novel agent for imaging T-cell activation with PET. 0*Mol Imaging Biol*. 2011;13(5):812–818.
34. Franc BL, et al. In vivo PET imaging of the activated immune environment in a small animal model of inflammatory arthritis. *Mol Imaging*. 2017;16:1536012117712638.
35. Sagiv-Barfi I, et al. Eradication of spontaneous malignancy by local immunotherapy. *Sci Transl Med*. 2018;10(426):aan4488.
36. Shrimali RK, et al. Concurrent PD-1 blockade negates the effects of OX40 Agonist antibody in combination immunotherapy through inducing T-cell apoptosis. *Cancer Immunol Res*. 2017;5(9):755–766.
37. Carboni S, Aboul-Enein F, Waltzinger C, Killeen N, Lassmann H, Peña-Rossi C. CD134 plays a crucial role in the pathogenesis of EAE and is upregulated in the CNS of patients with multiple sclerosis. *J Neuroimmunol*. 2003;145(1-2):1–11.
38. Kotani A, et al. Correlation of peripheral blood $OX40^+(CD134^+)$ T cells with chronic graft-versus-host disease in patients who underwent allogeneic hematopoietic stem cell transplantation. *Blood*. 2001;98(10):3162–3164.
39. Paz Morante M, et al. Activation-associated phenotype of CD3 T cells in acute graft-versus-host disease. *Clin Exp Immunol*. 2006;145(1):36–43.
40. James ML, et al. Imaging B cells in a mouse model of multiple sclerosis using 64Cu-rituximab PET. *J Nucl Med*. 2017;58(11):1845–1851.
41. Krieg AM, et al. CpG motifs in bacterial DNA trigger direct B-cell activation. *Nature*. 1995;374(6522):546–549.